The Astrophysical Journal, 982:101 (10pp), 2025 April 1 https://doi.org/10.3847/1538-4357/adb629

Plasma Instability Evolution and Particle Heating in the Foot Region of Perpendicular Shocks in Young Supernova Remnants

K. F. F. Law[1], S. Fujioka[1,2], and Y. Ohira[3]
[1] Institute of Laser Engineering, Osaka University, 2-6 Yamada-oka, Suita, Osaka, 565-0871, Japan
[2] National Institute for Fusion Science, 322-6 Oroshi-cho, Toki, Gifu, 509-5202, Japan
[3] Department of Earth and Planetary Science, The University of Tokyo, 7-3-1 Hongo, Bunkyo-ku, Tokyo, 113-0033, Japan
Received 2024 August 2; revised 2025 February 7; accepted 2025 February 11; published 2025 March 21

Abstract

Particle acceleration from collisionless shocks is a key mechanism in the generation of cosmic rays. In particular, shocks in young supernova remnants (SNRs) are considered to be a major source of galactic cosmic rays. This study investigates the early-stage plasma instability evolution and subsequent electron and ion heating in the foot region of high-Mach-number perpendicular shocks in young SNRs, using 2D particle-in-cell simulations. Unlike previous simulations that cover larger regions of the shock structure—including the downstream, shock, and upstream regions—our simulations are local, limited to the shock transition region, and focus on practical parameters with a nonrelativistic shock velocity ($v \approx 0.02c$) and the standard mass ratio between protons and electrons. We examined scenarios with and without the presence of return protons, and our results reveal that the Buneman instability, followed by the ion two-stream instability, dominates the early electron-heating process. We observed long-lasting ion heating in the case without return protons and note that the Weibel instability did not emerge within the simulation time frame. These findings enhance the understanding of plasma behavior in young SNR shocks and suggest that local simulations with practical parameters are crucial for exploring electron-heating mechanisms, while also highlighting the conditions under which the Weibel instability may or may not emerge.

Unified Astronomy Thesaurus concepts: Supernova remnants (1667); Shocks (2086); Plasma astrophysics (1261)

1. Introduction

Expanding supernova ejecta drives a collisionless shock in the interstellar or circumstellar medium (CSM). X-ray observations show that electrons are heated to 0.1–1 keV ranges approximately, and some electrons are accelerated to the relativistic energies in the collisionless shocks of supernova remnants (SNRs). Since electrons efficiently emit photons compared with ions, first of all, we obtain information on the electrons in the system. Since electrons radiate more efficiently than ions in various emission processes, such as synchrotron radiation and bremsstrahlung, the first information we typically obtain from the system is about the electrons. By comprehensively understanding the heating and acceleration processes of electrons near collisionless shocks, we can achieve a deeper insight into various physical mechanisms in SNRs. Based on their observation, the cosmic-ray acceleration, magnetic field amplification, magnetization, density, and shock velocity could be investigated to a greater extent, based on the buildup of knowledge of the physical mechanisms we have.

Depending on the directionality, magnetized collisionless shocks are categorized into two types: perpendicular or parallel shocks. They are defined by the relation between the shock normal direction and the upstream magnetic field direction. So far, many studies of the heating and acceleration of electrons have been conducted, especially by using particle simulations of plasma (T. Amano et al. 2022; J. C. Raymond et al. 2023). Since the shock transition region of the perpendicular shock has a typical scale length similar to the gyroradius of protons, which is generally shorter than that for parallel shocks, numerical studies on perpendicular shocks are less computationally expensive. In addition, for SNRs of core-collapse supernovae, Faraday rotation observation has suggested that the magnetic field in the CSM is expected to have the Parker spiral structure (L. Harvey-Smith et al. 2010). In this case, the shock wave would be a perpendicular shock in most regions of SNRs propagating to the CSM. For these reasons, many studies have focused on the perpendicular shock (N. Shimada & M. Hoshino 2000; M. Hoshino & N. Shimada 2002; T. Amano & M. Hoshino 2007, 2009; Y. Matsumoto et al. 2015, 2017; A. Bohdan et al. 2020). In perpendicular shocks, a fraction of the upstream protons are reflected and return to the shock front via the upstream magnetic field (M. Leroy 1983). As a source of anisotropy in the momentum space, the reflected protons excite different types of kinetic instabilities in the plasma. P. J. Cargill & K. Papadopoulos (1988) proposed a two-stage electron-heating mechanism, consisting of the Buneman instability (O. Buneman 1958) and ion acoustic instability (S. Ichimaru & T. Nakano 1973), both of which are electrostatic kinetic plasma instabilities excited by the reflected ions. They concluded that shocks in young SNRs heat electrons to $T_e/T_p \sim 0.2$, but the temperature ratio is larger than the observed value of $T_e/T_p \lesssim 0.05$ (P. Ghavamian et al. 2013; J. C. Raymond et al. 2023) for young SNRs, where T_e and T_p are the electron and proton temperatures, respectively. In this paper, we call this discrepancy the previous overheating problem.

On the other hand, for relativistic unmagnetized shocks, simulations show that electrons are efficiently heated to almost the equipartition level (A. Spitkovsky 2008), where $T_e \sim T_p$. This is consistent with observations of the afterglow of gamma-ray bursts and is well understood theoretically (A. Vanthieghem et al. 2022). However, for other types of collisionless shocks, the electron-heating process has not been understood

theoretically or observationally. Many recent simulations of SNR shocks (A. Bohdan et al. 2020; A. Vanthieghem et al. 2024) show that the ion acoustic instability does not play an important role in electron heating but, instead, the Weibel instability, which is an electromagnetic mode excited by the reflected protons, enhances the electron heating, resulting in $T_e/T_p \gtrsim 0.1$. This is again larger than $T_e/T_p \sim 0.05$ in young SNR shocks (J. C. Raymond et al. 2023).

Nevertheless, those simulations do not completely align with the actual situation in young SNR shocks: in terms of the shock velocity, faster values, such as $v_{sh}/c \sim 0.263$ in A. Bohdan et al. (2020), and relativistic shocks, as studied in A. Spitkovsky (2007, 2008), have often been employed in simulations to reduce the computational cost or to focus on different physical scenarios. High shock velocities directly enhance the growth rate of the ion Weibel instability, which depends not only on the plasma frequency but also explicitly on the shock velocity, $\gamma_W \propto v_{sh}/c$. This contrasts with other instabilities, such as the Buneman and ion two-stream instabilities, where their growth rates are indirectly enhanced by the shock velocity through the plasma frequency. Furthermore, as shown by A. Bret (2009) and A. Bret et al. (2010), such parameters can significantly alter the hierarchy of instabilities, with oblique modes often dominating at a realistic ion-to-electron mass ratio ($m_p/m_e = 1836$), as demonstrated in Y. Ohira & F. Takahara (2008). Regarding the magnetic field, stronger initial conditions, such as $v_{sh}/v_A \sim 22.6-68.7$ in A. Bohdan et al. (2020), where v_A is the Alfvén velocity, have been used to study magnetic reconnection phenomena in the perpendicular shock. These values amplify the magnetic field's influence on plasma dynamics but suppress the development of self-generated turbulence driven by the Weibel instability, which is critical for particle acceleration in low-field conditions. Finally, simulations often adopt an artificially reduced ion-to-electron mass ratio, such as $m_p/m_e \sim 50-400$ in A. Bohdan et al. (2020) and $m_p/m_e \sim 100$ in A. Spitkovsky (2007), to make computationally intensive plasma interactions more feasible. This choice reduces the scale separation between ion and electron dynamics, affecting the growth rates of instabilities such as the Buneman instability and the ion two-stream instability.

Currently, it is not feasible to simulate a whole shock structure of an SNR shock by a plasma particle simulation with a complete set of physical parameters closer to observation-derived estimations ($v_{sh}/c \sim 0.01$, $v_{sh}/v_A \sim 100$, and $m_p/m_e = 1836$). However, there are other numerical approaches to understanding electron heating and acceleration in SNR shocks, in which the simulation region is limited to the shock transition region, rather than solving the entire shock structure (Y. Ohira & F. Takahara 2007, 2008). Although a model of the shock transition region is required and any physics outside the limited region cannot be solved, the smaller computational domain allows for calculations with practical parameters, such as $v_{sh}/c \sim 0.01$, $v_{sh}/v_A > 100$, and $m_p/m_e = 1836$. Y. Ohira & F. Takahara (2007, 2008) showed by a local plasma particle simulation with practical parameters that the ion two-stream instability increases only the proton temperature before the ion acoustic instability occurs, so that the ion acoustic instability, which is the origin of the previous overheating problem, is stabilized. As a result, electrons are heated to $T_e/T_p \sim (128/3)(m_e/m_p) \sim 0.023$, which is almost consistent with observations of young SNRs.

The growth rate of the ion two-stream instability, $\gamma_{IT} = (2\sqrt{2}/16)^{1/3}(n_{p,ref}/n_p)^{1/3}\omega_{pp}$ (Y. Ohira & F. Takahara 2008), is larger than that of the ion Weibel instability, $\gamma_W = (2v_{sh}/c)(n_{p,ref}/n_p)^{1/2}\omega_{pp}$ (R. C. Davidson et al. 1972) in a practical parameter set of young SNRs, but the relationship between their growth rates is reversed for the parameter set that previous global shock simulations have used, where $n_{p,ref}$, n_p, and ω_{pp} are the densities of the reflected protons and upstream protons and the plasma frequency of the upstream protons, respectively. Y. Ohira & F. Takahara (2007, 2008) used an electrostatic simulation, which did not solve electromagnetic modes such as the Weibel instability. Therefore, whether the ion Weibel instability occurs after the saturation of the ion two-stream instability has not been understood yet for a practical parameter set of young SNRs. In other words, the current overheating problem has not been investigated by any local plasma particle simulation that solves electromagnetic modes yet. Furthermore, Y. Ohira & F. Takahara (2007, 2008) used a steady-state model of the transition region of the perpendicular shock, where there are three proton populations: upstream, reflected, and returning protons. Since high-Alfvén-Mach-number shocks exhibit periodic behavior over time (the so-called shock reformation), upstream protons are reflected periodically (K. B. Quest 1985; Z. Yang et al. 2020). The reflected protons from the shock and the return protons (gyrated reflected protons) are then not necessarily in the region simultaneously.

In this paper, we study the evolution of plasma instabilities in collisionless plasma, modeling the foot region in a collisionless perpendicular shock, by performing 2D full particle-in-cell (PIC) simulations. First, we perform simulations with a pair of counterstreaming proton populations. One population represents the reflected protons from the shock, while the other represents the returning protons after completing their gyration. These proton populations are set within a background proton–electron plasma. Here, we perform full PIC simulations as opposed to the electrostatic PIC simulations employed in the previous relevant study (Y. Ohira & F. Takahara 2007, 2008), to include electromagnetic modes as well as electrostatic modes. In order to model a certain phase of the shock reformation, we perform another simulation, considering a single population of reflected protons entering the region, by excluding the existence of return protons. The simulation setup and results are presented in Sections 2 and 3. We then discuss the plasma heating and stability of the Weibel instability in Sections 4 and 5. Finally, we summarize this work in Section 6.

2. Simulation Setting

In this work, we restrict the simulation box to a small part of the collisionless perpendicular shock system, instead of solving the dynamics of the whole shock structure, including both upstream and downstream regions. In the case of a perpendicular shock, some protons are reflected from the shock front and eventually return, due to their gyration under the upstream magnetic field. We refer to these as reflected protons and return protons. Here we focus on the reflection and return of protons, because electrons, with their much smaller gyroradii, do not meet the conditions for reflection and instead tend to pass through the shock front, where they are primarily heated or accelerated. The foot region is part of the upstream side of the shock transition region, where the reflected protons gyrate, with a spatial size of approximately the gyroradius of the reflected protons. Our simulation considers the physical situation inside

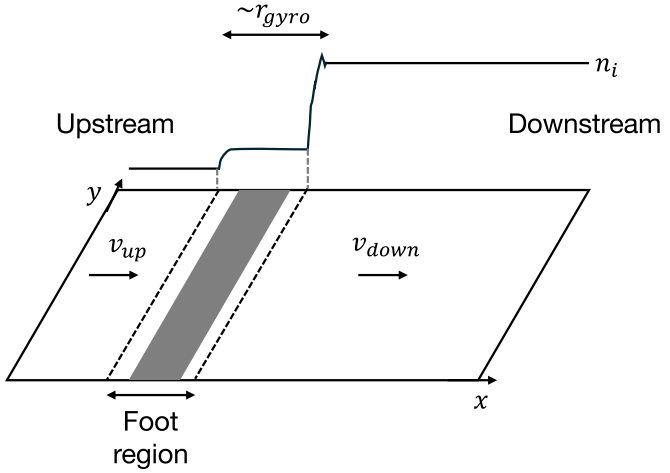

Figure 1. Schematic representation of the simulated region in the foot of the perpendicular shock. The gray area represents the simulation box. The broken line at the top of the figure illustrates the variation in ion density n_i schematically. The upstream and downstream regions, as well as the typical scale of the ion gyroradius $r_{\rm gyro}$, are indicated.

the foot region, with the whole simulation box located in a small portion of the entire foot region. By this approach, we are able to incorporate practical physical parameters into the numerical study, including the real proton-to-electron mass ratio and nonrelativistic shock velocity $v_{\rm sh}/c = 0.02$, which are both computationally expensive.

We perform numerical simulations to understand the heating process of electrons and protons in the shock foot region, using a 2D, three-velocity PIC simulation code, Wuming (T. Amano et al. 2024), originally developed for collisionless shock simulations (Y. Matsumoto et al. 2015). This means that while the spatial domain is restricted to two dimensions (x and y), the velocity and momentum components are fully defined in three dimensions (v_x, v_y, and v_z). Considering the collisionless nature of the astronomical plasma in our scope, collision effects are not included in our simulations.

The simulation is performed in 2D Cartesian coordinates, with the x-direction being defined as the shock normal pointing toward the upstream direction (away from the shock front). We apply the periodic boundary condition on both dimensions. The whole size of the simulation box is $60c/\omega_{\rm pe} \times 5c/\omega_{\rm pe}$ along the x- and y-directions, respectively, where $\omega_{\rm pe}$ is the electron plasma frequency. To facilitate comparisons, Figure 1 provides a schematic overview of the simulation region. The length of each cell and time step are $\Delta x = \Delta y = 5 \times 10^{-3}(c/\omega_{\rm pe})$ and $\Delta t = 2.5 \times 10^{-3}\omega_{\rm pe}^{-1}$. In this study, we adopt the standard proton-to-electron mass ratio $m_{\rm p}/m_{\rm e} = 1836$, which reflects the dominant composition of the interstellar medium, primarily consisting of hydrogen plasma. The simulation is performed until $t = 6400\omega_{\rm pe}^{-1}$, which is still shorter than the timescale of the ion gyration motion. While previous studies, such as Y. Ohira & F. Takahara (2008), have suggested that the initial background magnetic field may not significantly influence the temperature evolution, this conclusion is based on simplified assumptions of homogeneous magnetic fields and densities, without considering turbulence or spatial variations. These simplifications may limit the applicability of these results to more realistic scenarios, where such factors could play a role in the development of plasma instabilities. In this study, we have chosen to exclude the initial background magnetic field, for simplicity, and to focus on the primary plasma instabilities in the foot region of the shock. While weak magnetic fields or turbulence could influence the development of such instabilities in more complex astrophysical environments, the absence of an initial magnetic field in our simulations allows us to isolate and better understand the behavior of key instabilities, such as the Buneman and ion acoustic instabilities, under controlled conditions. In each cell, there are initially 96 macroparticles for both electrons and protons. For protons, this includes the background population as well as the reflected (and returning, if present) protons, with the total number of protons in all populations summing to 96 per cell. Prior to setting this value, we conducted preliminary computations to evaluate how the number of macroparticles per cell influences the overall electric field energy density in the simulation, up to $t = 5000\omega_{\rm pe}^{-1}$. We found that values below 30 ppc led to significant numerical heating effects, while for values of 30 ppc or higher, numerical heating was minimized and did not further decrease with increasing macroparticles per cell. Based on these tests, we adopted 96 ppc, to ensure that numerical heating remains at a minimal level throughout the simulation. The initial momentum distribution of each component is in a Maxwellian distribution with the same temperature $T = 1$ eV and with a different drift velocity. Under these simulation conditions, we examine two different situations: the case with return protons and another case without return protons.

2.1. Case A: With Return Protons

In the case with return protons, the plasma consists of a single population of electrons and three populations of protons, representing background electrons, background protons, reflected protons flowing toward upstream, and returning protons flowing toward downstream. The particle number density is initially homogeneous in the whole simulation box for all particle species, with the relations $n_{\rm p} = 2n_{\rm e}/3$ and $n_{\rm ref} = n_{\rm ret} = n_{\rm e}/6$, where the subscripts "p," "e," "ref," and "ret" represent background protons, background electrons, reflected protons, and returning protons, respectively. To model the protons being reflected from the shock front entering the foot region, the reflected protons have a drift velocity of $v_{\rm d} = 2v_{\rm sh} = 0.04c$ (representing the shock velocity $v_{\rm sh} = 0.02c$) with respect to the upstream protons, while the returning protons have a drift velocity of $-v_{\rm d}$ along the same axis. No initial velocity is assigned in the y-direction, as the drift motion is assumed to occur only along the x-axis. The simulation is set up in the rest frame of electrons, where the initial momentum distribution of the protons in the simulation is shown in Figure 2 (as the black dashed–dotted line).

The simulation setup in this run is basically similar to that in the previous related work (Y. Ohira & F. Takahara 2008), with the following differences. First, this simulation is performed by the full PIC code Wuming. Unlike the electrostatic PIC simulations in the previous work, this study also solves for the evolution of self-induced magnetic fields along with electric fields. Second, the initial temperature of all species has been reduced to approximately half of the previously used value of 1.75 eV, in order to better match observed values. In addition, the simulation box size and simulation time are extended from those in the previous work, to further investigate the plasma heating.

2.2. Case B: Without Return Protons

In the case without return protons, the proton population representing the returning protons is removed, to model the

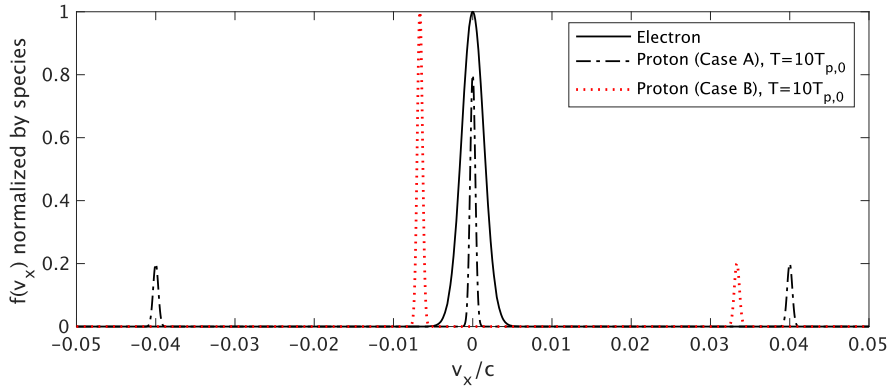

Figure 2. Distribution of the initial particle velocity along the x-axis in the PIC simulation. In this plot, the widths in the proton populations are exaggerated by setting the temperature as 10 times the simulation initial value, for the purpose of improving visibility.

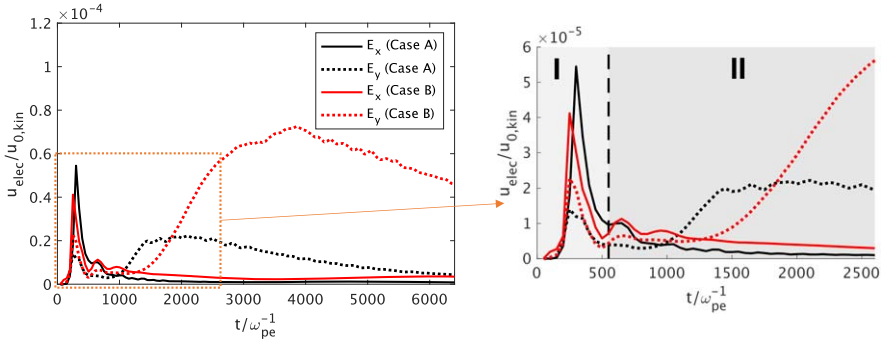

Figure 3. Time evolution of the energy density of the electric field until $t = 6400\omega_{pe}^{-1}$, the end of the simulation. The black and red curves represent Case A (with return protons) and Case B (without return protons), respectively. For each case, the solid and dotted lines represent E_x and E_y, respectively. A zoomed-in view of the time range $t = 0$ to $2600\omega_{pe}^{-1}$ is shown to highlight the early-time evolution of the energy density. The highlighted regions correspond to two distinct phases: Region I, dominated by the rapid growth of the Buneman instability; and Region II, characterized by the growth and subsequent decay of E_y due to the ion two-stream instability.

corresponding situation that occurred during shock reformation. In this case, the plasma consists of a single population of electrons and two populations of protons, representing background electrons, background protons, and the reflected protons flowing toward the upstream direction, where both densities are given by $n_p = 5n_e/6$ and $n_{ref} = n_e/6$. In addition, the upstream electrons have a relative drift velocity of $v_d(n_{ref}/n_e) = v_d/6$, with respect to the upstream protons, to satisfy the current neutrality condition at the beginning of the simulation run, ensuring that the simulation remains in the rest frame of the background electrons, as in the other case. The initial momentum distribution of the protons in the simulation is shown in Figure 2 (as the red dotted line).

3. Simulation Results

No exponential growth of magnetic fields via the Weibel instability was observed in our simulation until $t = 6400\omega_{pe}^{-1}$, even though the growth time is expected to be about $2600\omega_{pe}^{-1}$ in the initial condition. A more detailed discussion of this point can be found in Section 5.

The time evolution of the electric field energy density separated by components, averaged throughout the whole simulation box, is plotted in Figure 3. For both cases, the electric field energy density is normalized by the kinetic energy density at $t = 0$ corresponding to each case. The initial kinetic energy density differs between the two cases, with Case A having 2.4 times the kinetic energy density of Case B. Within the initial kinetic energy density, the contributions from the drift velocity are dominant, even though each population has a finite initial temperature.

Despite the differences in the simulation setting from the work in Y. Ohira & F. Takahara (2008), the evolution of the electric field in the case with return protons showed many common features with those reported in the work. For $t < 250\omega_{pe}^{-1}$ (in Region I, highlighted in Figure 3), both E_x and E_y rapidly grow, indicating the Buneman instability's early-stage evolution. E_x keeps decaying until the end of the simulation, while the E_y component rises again from $t \sim 1000\omega_{pe}^{-1}$ (in Region II, highlighted in Figure 3). After reaching its peak around $t = 1500\omega_{pe}^{-1}$, the decay of the E_y component started at $t \sim 2500\omega_{pe}^{-1}$. These features are basically the same as the previous result, while in this work, the disappearance of both components was observed, benefited by the longer simulation time. These features are also observed in the case without return protons, while the timings are different. The time evolutions of the temperatures evaluated from each species are shown in Figure 4. Here, the temperature of the species is defined as $T_s = m_s\langle(v - \langle v\rangle)^2\rangle/2k_B$ for each population s, with the population average velocity $\langle v\rangle$ being computed at each snapshot from the simulation data, where k_B is the Boltzmann constant. In both cases, rapid electron heating is observed at the beginning of the simulation for $t < 250\omega_{pe}^{-1}$. The majority of protons have not strongly heated yet, which is the typical feature of the Buneman instability dominant phase. Notably, in contrast to the background protons, significant heating was observed in the reflected and returning protons. In

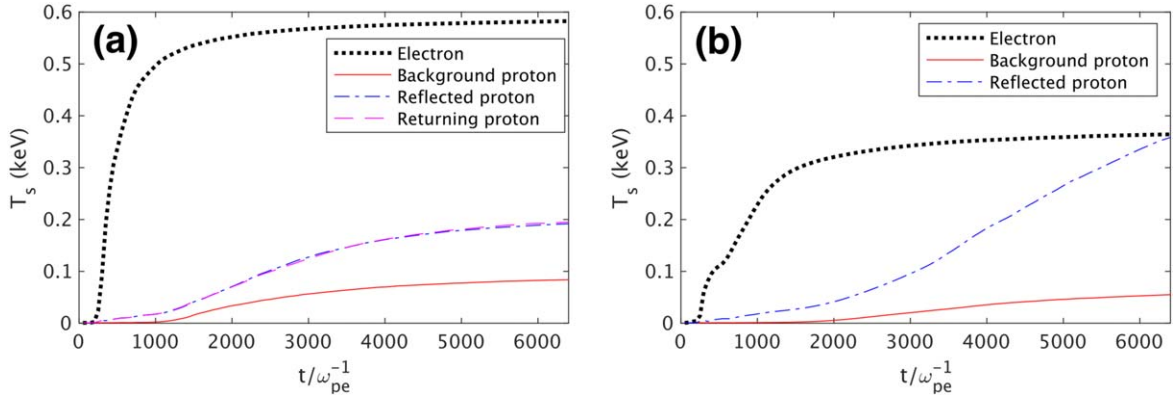

Figure 4. Time evolution of the species temperature in: (a) Case A; and (b) Case B. The temperatures of the electrons, background protons, reflected protons, and returning protons are represented by the black dotted line, red solid line, blue dashed–dotted line, and magenta dashed line, respectively. For each species, the species temperature is evaluated in the rest frame of the particle species at each snapshot.

both cases, $T_{\rm p,ref}$ exceeds $10T_0$ at $t = 1000\omega_{\rm pe}^{-1}$, which is 1 order of magnitude larger than the initial $T_{\rm p,ref}$. Nevertheless, the relation $T_{\rm e} \gg T_{\rm p}$, triggered by the electron heating from the Buneman instability, still holds at this stage, which is the situation where the Buneman instability has stabilized and a different type of instability starts to dominate. From $t \sim 1000\omega_{\rm pe}^{-1}$ ($t \sim 1500\omega_{\rm pe}^{-1}$ for the case without return protons), the background proton temperature starts rising significantly, together with an increase in the temperature of the reflected protons (and returning protons, in the case with return protons). In both cases, the temperature of the background protons shows saturation at the end of the simulation, approximately $T_{\rm p} \sim T_{\rm e}/6$. However, the temperature of the reflected protons showed a very different evolution. Similar to the analysis made in previous literature (T. N. Kato & H. Takabe 2010), the heating of the reflected protons eventually stops as $T_{\rm p,ref}$ approaches $\sim 0.3T_{\rm e}$ in the case with return protons, while the heating of the reflected protons in the case without return protons did not show any tendency for saturation in our simulation. As a result, the reflected proton temperature $T_{\rm p,ref}$ reaches the value of $T_{\rm e}$ at the end of the simulation, $t = 6400\omega_{\rm pe}^{-1}$.

The electric field along the drift direction E_x sampled from a portion of the whole simulation box at $t = 250\omega_{\rm pe}^{-1}$, during the first stage of electron heating, and its power spectra are shown in Figure 5. The wavenumbers k_x and k_y are normalized by $k_0 = \omega_{\rm pe}/v_{\rm d}$, where the Buneman instability has a maximum growth rate in the cold limit. Being common in both cases, E_x shows a wavy structure, localized in k_x and extending in the k_y direction. This is consistent with the feature of the Buneman instability that strongly depends on k_x, while k_y is only constrained by the effect of finite temperature that stabilizes large wavenumber modes. E_y is then analyzed in the same way at $t = 2000\omega_{\rm pe}^{-1}$ in the case with return protons and $t = 4000\omega_{\rm pe}^{-1}$ in the case without return protons, which are taken around the peak value of E_y as observed in Figure 3. From the power spectrum of E_y, a common component is observed, concentrating at a small value of $k_x \ll \omega_{\rm pe}/v_{\rm d}$ and extending along the k_y direction for $k_y < k_{\rm D,e} \sim 8k_{\rm Bun}$, where $k_{\rm D,e} = \omega_{\rm pe}/v_{\rm the,e}$ is the wavenumber corresponding to the Debye length. This agrees with the wavenumber corresponding to the maximum growth rate, obtained by linear analysis in Y. Ohira & F. Takahara (2008) for the ion two-stream instability under the condition $T_{\rm e}/T_{\rm p} = 100$. This implies that the oblique modes also grow strongly in these situations, with the significantly larger amplitude in E_y (compared to E_x) also showing the obliqueness of the excited electric field. In the region with larger k_x, the E_y power spectra revealed distinct features compared to those observed at smaller k_x values. In Case A, only some remains of the Buneman instability are observed at $k_x/k_0 = 1$ and 2. In Case B, a component with larger broadening in k_x is observed at $k_y < 2k_0$.

4. Heating and Isotropization

From the two cases studied in independently conducted PIC simulations with practical physical parameters, we observed consistent behavior in the evolution of the electric field. In both cases, the Buneman instability grows in the early stage, resulting in the rapid heating of electrons. After the decay of the E_x component and the Buneman instability, the growth of the E_y component and ion heating were observed in both cases. Here, the most significant difference between the two cases appears: when the background component and the reflected component(s) of the protons were analyzed separately, we observed that the reflected component is heated to the same temperature as the electron temperature when the return component is absent. In contrast, the heating of the reflected component saturates at about $0.3T_{\rm e}$, as well as the return component, when the latter exists. Our results indicate that reflected protons continue to heat up to temperatures comparable to $T_{\rm e}$ in the absence of return protons. This long-lasting heating may be driven by the sustained E_y component from the ion two-stream instability and potentially by Landau resonance, although this remains speculative without further frequency analysis. This process may transfer the kinetic energy in the beam component to its thermal component, resulting in the continuous heating of reflected protons in our simulation. However, a more detailed analysis, such as a frequency analysis in future high-resolution simulations in the time domain, would be necessary to confirm specific mechanisms such as Landau resonance.

The power spectrum of E_x at the first stage of heating showed a typical feature that is identified as the result of the Buneman instability growth, in both cases with and without return protons. On the other hand, the power spectrum of E_y at the second stage of heating provides more clues about the ion heating, by showing differences between the two cases. For the simulation with return protons, only the almost perpendicular

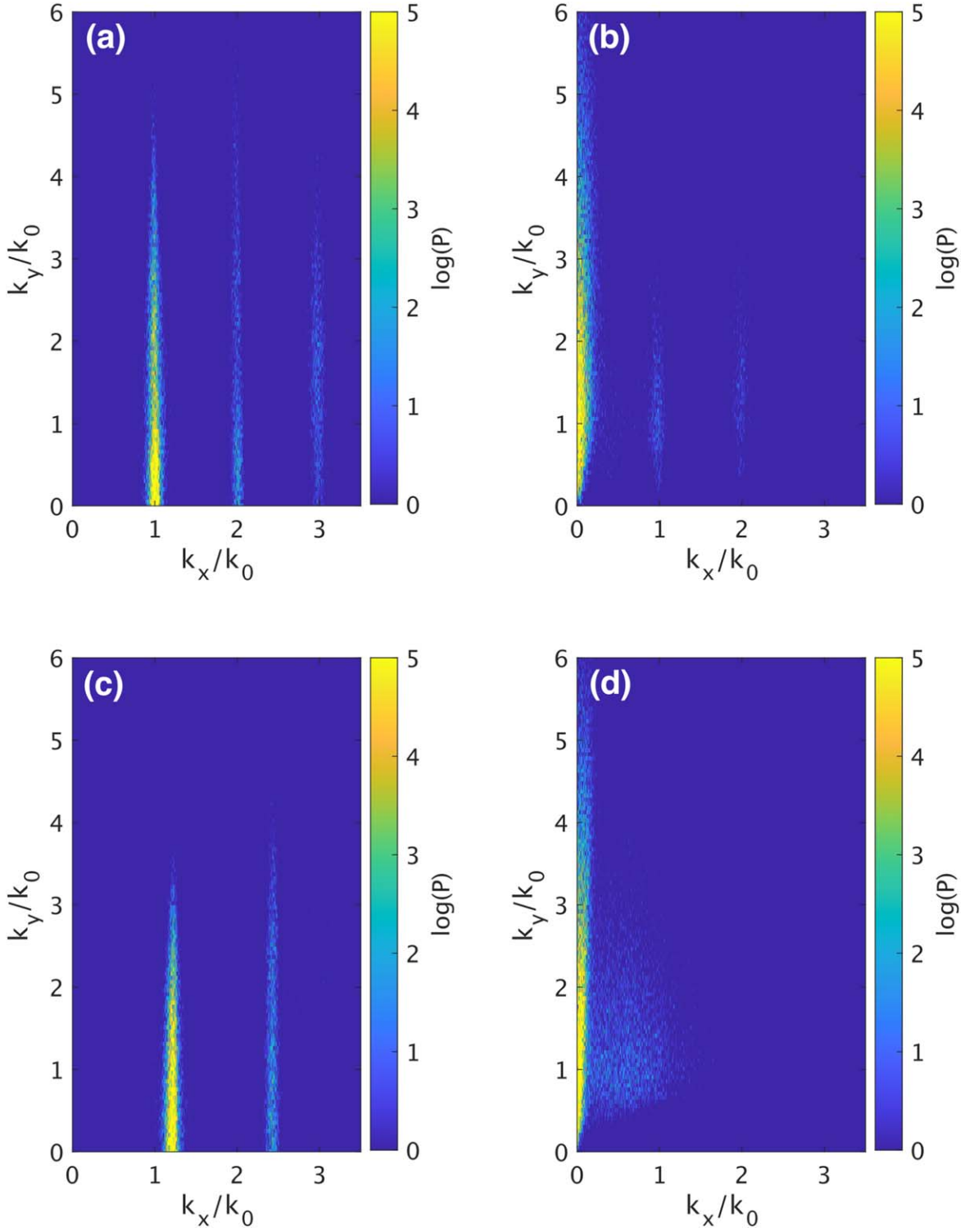

Figure 5. (Upper) Power spectrum P of: (a) E_x at $t = 250\omega_{pe}^{-1}$; and (b) E_y at $t = 2000\omega_{pe}^{-1}$, in Case A. (Lower) Power spectrum P of: (c) E_x at $t = 250\omega_{pe}^{-1}$; and (d) E_y at $t = 4000\omega_{pe}^{-1}$, in Case B. Both k_x and k_y are normalized by $k_0 = \omega_{pe}/v_d$, the wavenumber where the Buneman instability has a maximum growth rate in the cold limit. The power spectra are normalized by $(m_e\omega_{pe}c/e)^2$.

(y-direction) component, identified as the result of the ion two-stream instability, was observed from the power spectrum of E_y. When the return protons are absent from the simulation, another component with a smaller spectral density but a larger spread in the wavenumber domain was observed from the power spectrum, on top of the ion two-stream instability feature. This feature can be interpreted as a signature of ion acoustic instability, because k_x approximately centered at ω_{pe}/v_d (Y. Ohira & F. Takahara 2008). The presence of weak ion acoustic instability growth in the absence of return protons further underscores the distinct plasma behavior under different ion population conditions.

The temperature anisotropy is also an important factor in this situation, as it is known that the ion temperature anisotropy in

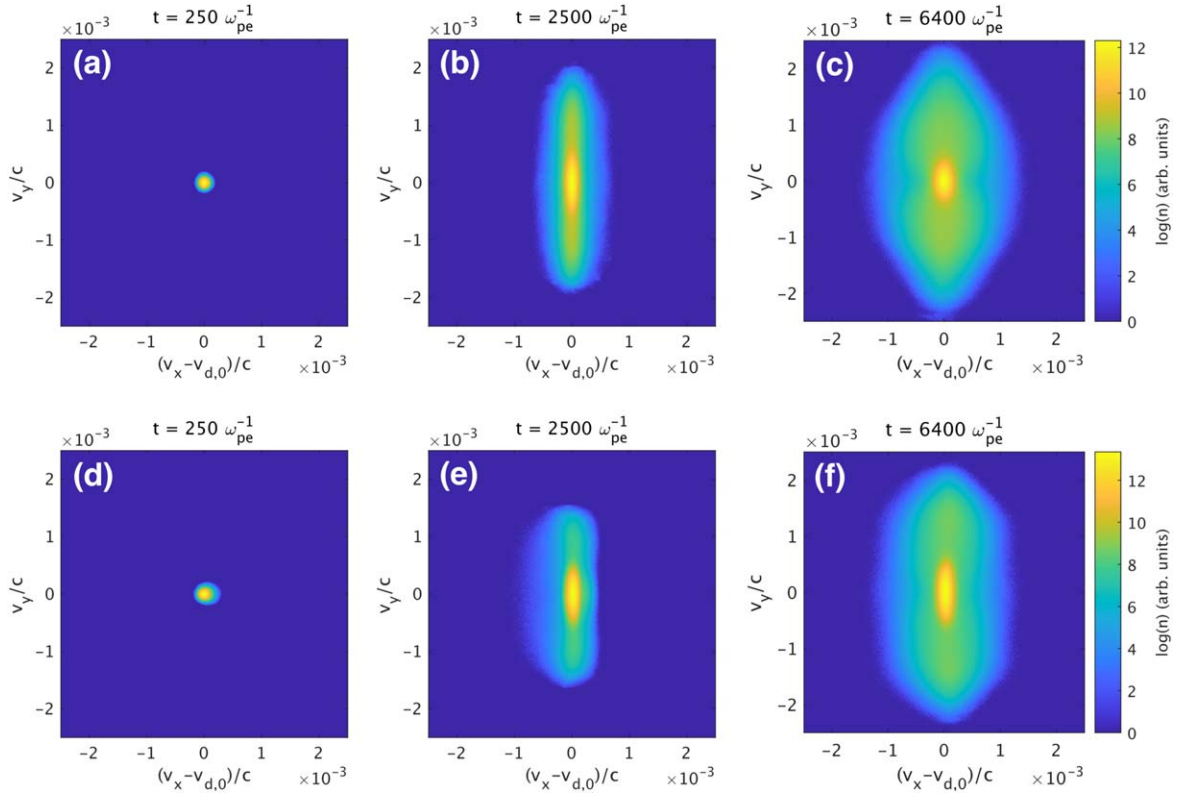

Figure 6. Phase diagram of the background protons, in Case A (upper panels) and Case B (lower panels). The initial value of the drift velocity $v_{d,0}$ of the species is subtracted from v_x.

plasma will excite the Weibel instability that contributes further heating. The velocity distribution of the proton components at different stages is plotted in Figure 6 for the background protons and in Figure 7 for the reflected protons. It is observed that for the background protons, the spread in the phase space is similar in both cases, for both the x- and y-components. This is consistent with the time evolution in both cases, shown in Figure 4. For the reflected protons, it is observed that the protons are heated in a way that the velocity spread along the y-direction is a few times larger than along the x-direction, in both cases with and without returning protons. At $t = 6400\omega_{pe}^{-1}$, the maximum spreads of v_x and v_y are approximately the same in both cases. Therefore, the significantly larger heating of reflected protons, in the case of the absence of returning protons, can be explained by a larger proportion of protons getting heated and a more flat-topped distribution, which can be observed from the difference between Figures 7(c) and (f).

The major contribution to the anisotropy in momentum space is the presence of the drift population, with drift velocity along the x-direction. Therefore, the ion heating with the larger velocity spread in the y-direction can be interpreted as the isotropization process. As shown in Figure 4, this isotropization process is close to saturation when the return protons exist in the system. In contrast, the isotropization is maintained at the end of our simulation for the case of the absence of the returning protons. The isotropization of the particle distribution in momentum space before the excitation of the Weibel instability affects its growth rate and the unstable wavenumber region. This, in turn, influences the forthcoming electron heating. We discuss this point in the next section.

5. Stability Analysis of Weibel Instability

In our local simulation with a practical parameter set for SNR shocks, we did not observe the growth of the Weibel instability. The largest growth rate and largest unstable wavenumber of the Weibel instability for the plasma in the initial condition are $\gamma_W = (v_{d,ref}/c)\omega_{p,ref}$ and $k_{max} = (\sqrt{2}\, v_{d,ref}/v_{th,ref})\omega_{p,ref}/c$ (R. C. Davidson et al. 1972), where $\omega_{p,ref} = (4\pi n_{p,ref} e^2/m_p)^{1/2}$, $v_{d,ref}$, and $v_{th,ref}$ are the plasma frequency, drift velocity, and thermal velocity of the reflected protons. The corresponding timescale, $\gamma_W^{-1} \approx 2600\ \ \omega_{pe}^{-1}$, and wavelength, $2\pi/k_{max} \approx 0.42\ \ c/\omega_{pe}$, are both smaller than our simulation time and box size in the y-direction. Thus, the Weibel instability results in magnetic field amplification, as long as the initial condition is maintained for the timescale of γ_W^{-1}. However, as shown in our simulation, the plasma is heated by the Buneman and ion two-stream instabilities before the Weibel instability grows, because of their larger growth rates compared to the Weibel instability, which changes the plasma condition with respect to the growth of the Weibel instability.

The Weibel instability is driven by the anisotropy of the particle distribution in the momentum space. In this case, the reflected protons (and return protons in Case A) in the foot region of collisionless perpendicular shocks have a drift velocity of the order of the shock velocity in the center-of-mass frame (the upstream electron rest frame), which creates the anisotropy. To understand the stability of the Weibel

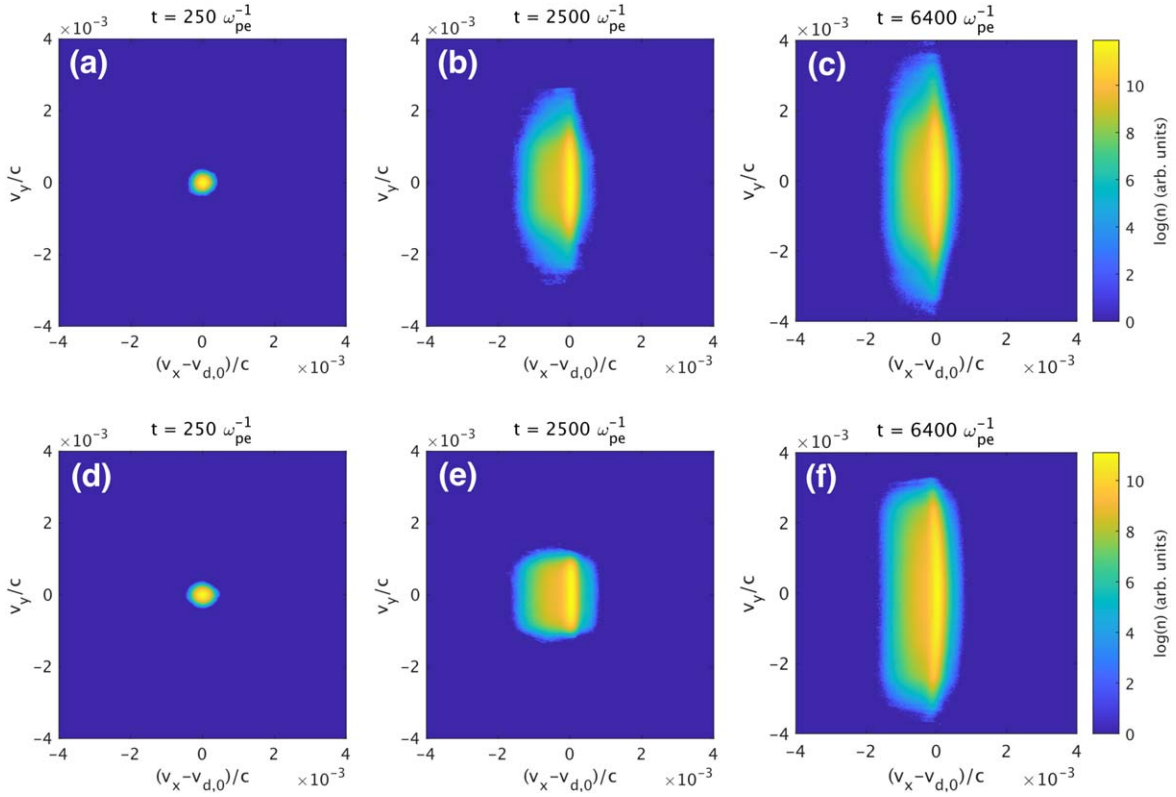

Figure 7. Phase diagram of the reflected protons, in Case A (upper panels) and Case B (lower panels). The initial value of the drift velocity $v_{d,0}$ of the species is subtracted from v_x.

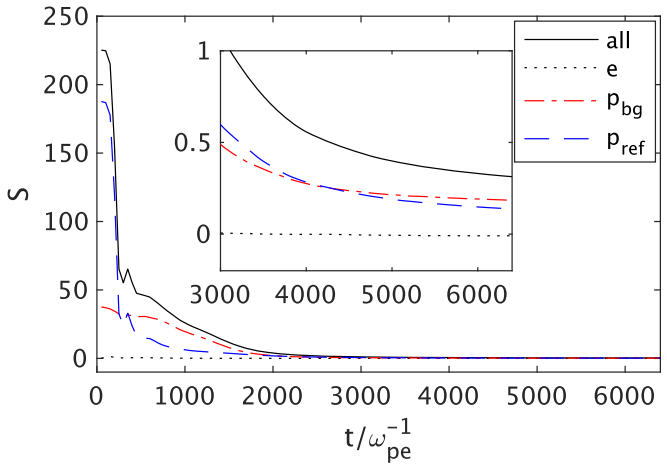

Figure 8. Time evolution of $S = \sum_j (\omega_{pj}/\omega_{pe})^2 \{[(T_{jx} + m_j v_{dj}^2)/T_{jy}] - 1\}$ in Case B. The electron component, background proton component, reflected proton component, and total value of S are represented as the black dotted, red dashed–dotted, blue dashed, and black solid lines, respectively.

instability, we calculate the total anisotropy in the system:

$$S = \sum_j \left(\frac{\omega_{pj}}{\omega_{pe}}\right)^2 \left\{\frac{(T_{jx} + m_j v_{d,j}^2)}{T_{jy}} - 1\right\}. \quad (1)$$

The condition of $S > 0$ is the necessary and sufficient condition for the Weibel instability to occur (R. C. Davidson et al. 1972). Figure 8 shows the time evolution of S in our simulation for case B. After the Buneman instability saturates ($t = 250\omega_{pe}^{-1}$), the total anisotropy decreases to about a quarter of the initial value. The total anisotropy then significantly drops to $\sim$0.5, about 10^{-3} of the initial value, and still decreases with time at the end of our simulation, because the upstream and reflected protons were continuously heated in the y-direction by the ion two-stream instability. The largest growth rate and largest unstable wavenumber of the Weibel instability at the end of our simulation are $\gamma_W \sim (4/27\pi)^{1/2}(v_{th,ref}/c)S^{1/2}\omega_{pe}$ and $k_{max} = S^{1/2}\omega_{pe}/c$ (C. Ruyer et al. 2017). The corresponding timescale and wavelength are $\gamma_W^{-1} \approx 7000\ \omega_{pe}^{-1}$ and $2\pi/k_{max} \approx 9\pi\ c/\omega_{pe}$, both of which exceed the simulation time and box size used in this work. This limitation likely explains why magnetic field amplification by the Weibel instability was not observed here. Therefore, observing such amplification would require not only longer simulation times but also a larger simulation domain in future studies.

As reflected and upstream protons are further heated in the direction perpendicular to the shock normal before the Weibel instability occurs, the time and length scales of the Weibel instability become longer. The electron magnetization by the background magnetic field could then play an important role (T. Jikei et al. 2024). If the timescale of the Weibel instability exceeds the proton gyro period, it may not develop in the foot region of perpendicular shocks in SNRs. Even though the Weibel instability occurs in the foot region, the saturation level of the Weibel instability also depends on the proton-to-electron mass ratio and shock velocity (T. Jikei & T. Amano 2024). Based on our analysis, for the Weibel instability to develop and influence particle heating, a simulation with twice the current timescale and approximately six times the lateral spatial scale would be required. Furthermore, due to the continuous heating of protons observed in this study, the growth rate of the Weibel instability would likely diminish, requiring an even larger and

longer simulation domain than this initial estimation. Therefore, such a larger full PIC simulation with an expanded parameter set is essential for conclusively determining the role of the Weibel instability in electron heating in the perpendicular shocks of young SNRs.

6. Summary

In this study, we have performed 2D full PIC simulations to investigate the evolution of plasma instabilities in the foot region of a collisionless perpendicular shock of young SNRs, focusing on the heating processes of electrons and protons in a practical parameter set of young SNRs. By simulating scenarios with and without the presence of returning protons, which correspond to a steady shock and an unsteady shock with reformation, we have explored the differences in dynamics and outcomes of these different situations on plasma heating. We have shown that under full PIC simulations taking electromagnetic modes into account, the heating process consists of an initial electron heating followed by ion heating, similar to previous results from electrostatic PIC simulations. The growth of the Weibel instability was not observed until the end of our simulation, $t = 6400\omega_{\rm pe}^{-1}$. For the situation without returning protons, the ion acoustic instability and long-standing ion heating by the ion two-stream instability are observed. Through the stability analysis of the Weibel instability, we have shown that the region in wavenumber space corresponding to Weibel instability growth is largely restricted by the proton heating in the y-direction, due to the highly oblique ion two-stream instability. This heating suppresses the growth rate and further extends the timescale for the observation of possible Weibel instability in such a system. Therefore, the shock reformation increases the temperature of the reflected protons, which reduces the growth rate and the unstable wavenumber region of the Weibel instability. As a result, less electron heating would be expected.

While our localized simulation approach provides valuable insights into early-stage plasma instabilities and heating mechanisms, it inherently omits certain physical processes that may arise in a more complete model of the shock transition region. For instance, larger-scale effects—such as the interplay of turbulence, changes in incoming particle characteristics, and additional plasma instabilities outside the simulation domain—cannot be captured in this setup. These limitations highlight the importance of carefully considering the model-dependent factors of the shock transition region when interpreting the results. Overall, our study provides an examination of the early electron- and ion-heating processes in the shock foot region of collisionless perpendicular shocks of young SNRs. By comparing the outcomes under different initial conditions, we have identified instabilities that govern the thermal dynamics of the plasma, as well as the role of shock reformation on the initial proton-heating process. As future work, full PIC simulations with the practical parameter set and extended temporal and spatial domains will be necessary to conclude whether or not the Weibel instability occurs in the perpendicular shocks of young SNRs and to capture additional physical effects that were beyond the scope of this study.

Acknowledgments

Preliminary computations were carried out on Cray XC50 at the Center for Computational Astrophysics, National Astronomical Observatory of Japan. This work was supported by MEXT, as the "Program for Promoting Researches on the Supercomputer Fugaku" (JPMXP1020200109), and used computational resources of the supercomputer Fugaku provided by the RIKEN Center for Computational Science (Project ID: hp230073). This research was supported by Japan Society for the Promotion of Science (JSPS) KAKENHI Grants (JP21H04487 and JP24H01805), the joint research project of the Institute of Laser Engineering, Osaka University (2022B2-061, 2023B2-030, and 2024B2-040), the MEXT Project for promoting the public utilization of advanced research infrastructure (Program for advanced research equipment platforms; JPMXS0450300021), and the JSPS Core-to-Core Program (JPJSCCA20230003).

Appendix
2D Electric and Magnetic Field Distributions at the End of the Simulation

To analyze the development of plasma instabilities, we present 2D spatial distributions of E_x, E_y, and B_z at $t = 6400\omega_{\rm pe}^{-1}$, the end of the simulation in this work. Figure 9 shows the results for Case A (top row) and Case B (bottom row), focusing on the range $20 \leqslant x/(c/\omega_{\rm pe}) \leqslant 25$. The electric field component E_y exhibits distinct structures in both cases. In particular, in Case B, a well-defined wave-like pattern develops. The dominant wave modes in Case B are almost perpendicular to the direction of the proton beam, though they are not fully aligned in the y-direction. This observation is consistent with the power spectrum analysis shown in Figure 5(d), where the power spectrum of E_y in Case B reveals the presence of modes with a small k_x and a broad spread in k_y, further supporting the identified wave structures.

The self-generated magnetic field, B_z, remains weak throughout the simulation. However, in Case B, its spatial distribution shows a certain degree of similarity to the wavy patterns observed in E_y. This suggests that the magnetic field is generated by the ion two-stream instability. The ion two-stream instability makes spatially narrow proton beams. Electrons cannot compensate for the proton current, because the width is much smaller than the electron inertial length scale, so the proton current directly generates magnetic fields. Thus, the ion two-stream instability excites a mode in which electromagnetic and electrostatic modes are coupled, rather than a purely electrostatic mode. However, the current of each proton filament is not large enough to generate strong magnetic fields, because the drift velocity and the filament width are small.

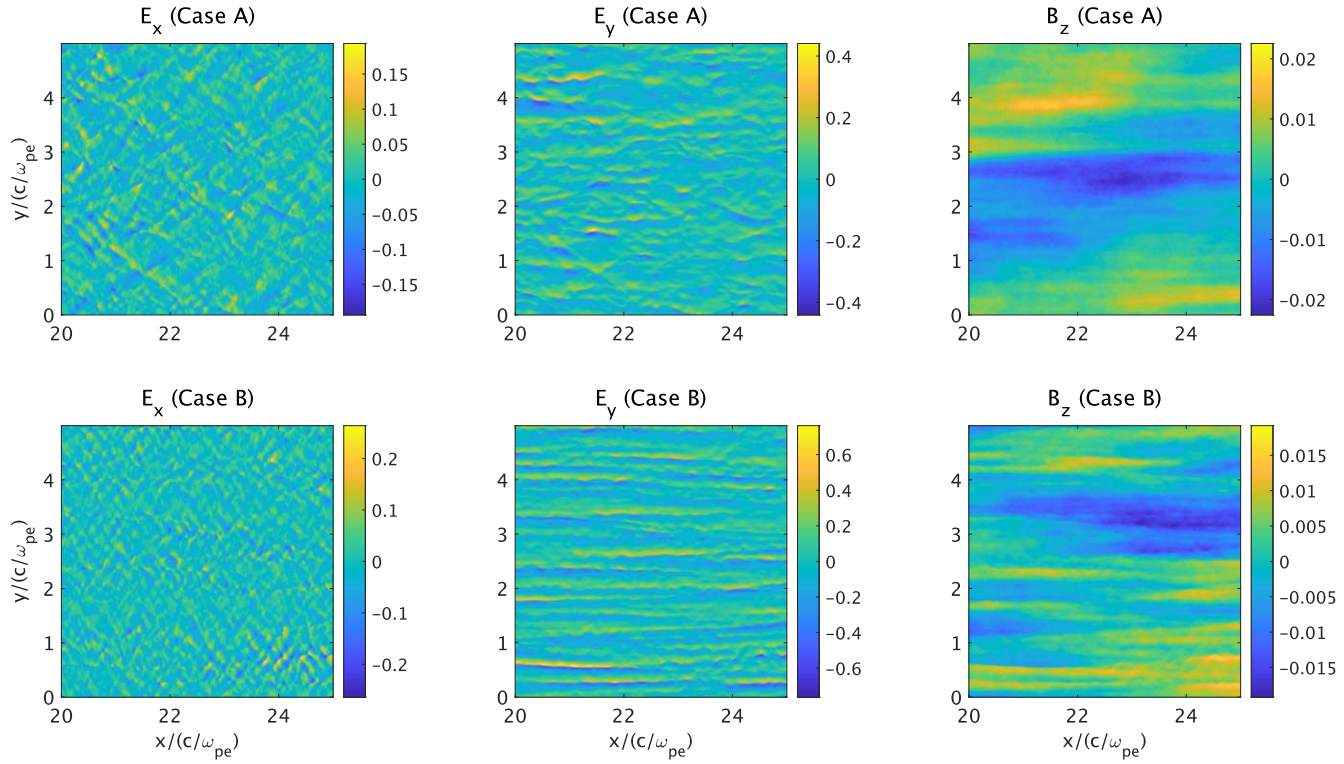

Figure 9. 2D distributions of E_x, E_y, and B_z at $t = 6400\omega_{pe}^{-1}$. The top row represents Case A (with return protons), and the bottom row represents Case B (without return protons). The spatial range is restricted to $20 \leqslant x/(c/\omega_{pe}) \leqslant 25$ for better visualization of the field structures.

ORCID iDs

K. F. F. Law https://orcid.org/0000-0002-5484-8870
S. Fujioka https://orcid.org/0000-0001-8406-1772
Y. Ohira https://orcid.org/0000-0002-2387-0151

References

Amano, T., & Hoshino, M. 2007, ApJ, 661, 190
Amano, T., & Hoshino, M. 2009, ApJ, 690, 244
Amano, T., Matsumoto, Y., Bohdan, A., et al. 2022, RvMPP, 6, 29
Amano, T., Matsumoto, Y., & Iwamoto, M. 2024, WumingCode/WumingPIC2D: v0.52, Zenodo, doi:10.5281/zenodo.10990576
Bohdan, A., Pohl, M., Niemiec, J., et al. 2020, ApJ, 904, 12
Bret, A. 2009, ApJ, 699, 990
Bret, A., Gremillet, L., & Dieckmann, M. E. 2010, PhPl, 17, 120501
Buneman, O. 1958, PhRvL, 1, 8
Cargill, P. J., & Papadopoulos, K. 1988, ApJL, 329, L29
Davidson, R. C., Hammer, D. A., Haber, I., & Wagner, C. E. 1972, PhFl, 15, 317
Ghavamian, P., Schwartz, S. J., Mitchell, J., Masters, A., & Laming, J. M. 2013, SSRv, 178, 633
Harvey-Smith, L., Gaensler, B., Kothes, R., et al. 2010, ApJ, 712, 1157
Hoshino, M., & Shimada, N. 2002, ApJ, 572, 880
Ichimaru, S., & Nakano, T. 1973, PThPh, 50, 1867
Jikei, T., & Amano, T. 2024, MNRAS, 531, 219
Jikei, T., Amano, T., & Matsumoto, Y. 2024, ApJ, 961, 157
Kato, T. N., & Takabe, H. 2010, ApJ, 721, 828
Leroy, M. 1983, PhFl, 26, 2742
Matsumoto, Y., Amano, T., Kato, T., & Hoshino, M. 2015, Sci, 347, 974
Matsumoto, Y., Amano, T., Kato, T. N., & Hoshino, M. 2017, PhRvL, 119, 105101
Ohira, Y., & Takahara, F. 2007, ApJL, 661, L171
Ohira, Y., & Takahara, F. 2008, ApJ, 688, 320
Quest, K. B. 1985, PhRvL, 54, 1872
Raymond, J. C., Ghavamian, P., Bohdan, A., et al. 2023, ApJ, 949, 50
Ruyer, C., Gremillet, L., Bonnaud, G., & Riconda, C. 2017, PhPl, 24, 041409
Shimada, N., & Hoshino, M. 2000, ApJL, 543, L67
Spitkovsky, A. 2007, ApJL, 673, L39
Spitkovsky, A. 2008, ApJL, 682, L5
Vanthieghem, A., Lemoine, M., & Gremillet, L. 2022, ApJL, 930, L8
Vanthieghem, A., Tsiolis, V., Spitkovsky, A., et al. 2024, PhRvL, 132, 265201
Yang, Z., Liu, Y. D., Johlander, A., et al. 2020, ApJL, 901, L6